Nebular and asteroidal modification of the iron isotope composition of chondritic components

E. Mullane [a,b,*], S.S. Russell [a,1], M. Gounelle [b,2]

[a] Impacts and Astromaterials Research Centre, Department of Mineralogy, The Natural History Museum, Cromwell Road, London, SW7 5BD, United Kingdom
[b] CSNSM, Université Paris 11, Bâtiment 104, 91405 Orsay Campus, France

Abstract

The Fe-isotope signatures ($\delta^{56}Fe_{IRMM}$ and $\delta^{57}Fe_{IRMM}$) of twelve chondrules, three Ca-, Al-rich inclusions (CAIs) and multiple matrix aliquots from two type 3 chondrites — Allende (CV3) and Chainpur (LL3) were measured by MC-ICP-MS. The mass-fractionation line for these samples is $\delta^{57}Fe_{IRMM} = (1.45 \pm 0.05) \cdot \delta^{56}Fe_{IRMM} - (0.01 \pm 0.02)$ with $R^2 = 0.9995$. Two processes appear to affect the Fe-isotope composition of these chondritic components. Initially, short-lived high-temperature events within the solar nebula drove isotopic signatures towards isotopically heavier compositions. Subsequently, metasomatism shifted isotopic signatures of chondrules and CAIs towards bulk-like compositions. The Fe-isotope composition of Allende matrix ($\delta^{56}Fe_{IRMM} = -0.07 \pm 0.02‰$, $n=6$) is similar to that of bulk Allende ($\delta^{56}Fe_{IRMM} = -0.05 \pm 0.05‰$). The range of Chainpur matrix compositions is $-0.03 \leq \delta^{56}Fe_{IRMM} \leq +0.02‰$. This relatively homogeneous matrix composition appears to be governed by metasomatic exchange of iron, although the possibility that matrix is heterogeneous on a scale smaller than the sample size cannot be ruled out. CAIs from Allende, in which iron has been metasomatically introduced from the matrix, are mainly unfractionated with respect to the bulk composition of Allende. The least altered CAI, which contains minor bulk FeO (0.4 wt.%), is isotopically lighter ($\delta^{56}Fe_{IRMM} = -0.16‰$) with respect to bulk Allende. This signature may reflect condensation of isotopically light iron in the nebula or preferential incorporation of the lighter iron isotopes contained within the matrix. Chondrule Fe-isotope compositions ($-1.33 \leq \delta^{56}Fe_{IRMM} \leq +0.65‰$) are driven by both high-temperature nebular events and subsequent metasomatic exchange. The relationship between compositional and isotopic signatures clearly points to an evaporation origin for type I chondrules, which are isotopically heavier than type II chondrules. Subsequent metasomatic

* Corresponding author. Current address: Department of Geology, The Field Museum, 1400 South Lake Shore Drive, Chicago, IL 60605, United States of America. Tel.: +1 312 665 7656; fax: +1 312 665 7641.
  E-mail addresses: emullane@fieldmuseum.org (E. Mullane), sarr@nhm.ac.uk (S.S. Russell), gounelle@csnsm.in2p3.fr (M. Gounelle).
[1] Tel.: +44 20 7942 5074; fax: +44 20 7942 5537.
[2] Current address: Laboratoire d'Étude de la Matière Extraterrestre, Muséum National d'Histoire Naturelle, 61 rue Buffon, 75005 Paris, France. Tel.: +33 1 69 155247; fax: +33 1 69 155008.

exchange with matrix iron has driven some chondrules (most notably the smaller chondrules) towards a bulk-like Fe-isotopic signature.

1. Introduction

The effects of nebular and asteroidal processing on the chemical and isotopic composition of chondritic components (e.g. chondrules, CAIs and matrix) have long been debated. We used Fe-isotopes ($\delta^{56}Fe_{IRMM}$ and $\delta^{57}Fe_{IRMM}$), measured by multiple collector inductively coupled plasma mass spectrometry (MC-ICP-MS) [1], to evaluate the effects of these processes on chondritic components from the Allende (CV3) carbonaceous chondrite and the Chainpur (LL3) ordinary chondrite. This brings together the results of preliminary reports [2–4].

The ability to precisely measure Fe-isotopes is a relatively new analytical development. Iron isotopes are gradually being characterized in a number of natural [e.g. [5–9]] and experimental [e.g. [10,11]] systems using MC-ICP-MS. However, studying the Fe-isotope systematics of extraterrestrial material is not a new endeavour. Fe-isotopes have previously been measured in extraterrestrial samples using thermal ionization mass spectrometry [12,13] and ion microprobe [14]. Apart from large mass-independent anomalies in ^{58}Fe identified in FUN inclusions [12], neither technique was sufficiently precise to measure Fe-isotope variations in the sub-permil range [13,14]. Recently, Fe-isotope mass-dependent fractionation in chondrules has been identified using MC-ICP-MS [5,7]. The results of the present study indicate that both nebular and asteroidal processing modify Fe-isotope compositions.

2. Samples and methods

2.1. Samples

Allende (ALL) and Chainpur (CHP) components are abbreviated as follows: chondrule = CL, Ca-, Al-rich inclusions = CAI, and matrix = MTX. Thus, chondrule 1 from Allende is ALL-CL-1. The Allende (CV3) samples consist of one bulk sample, nine chondrules, three CAIs, and six matrix aliquots. The Chainpur (LL3) samples comprise three chondrules, and two matrix aliquots. Although both Allende and Chainpur are petrologic type 3 chondrites, neither sample may have escaped nebular or parent body alteration [15].

2.2. Sample preparation and characterization

Chondrules and CAIs were handpicked from lightly crushed material. The samples were weighed and the dimensions of each chondrule and CAI were measured. Each object was subsequently split in two. One sub-sample was used for petrographical characterization. Textural characterization was made using a Phillips XL-30 FEG SEM, operated in backscatter detection mode. Modal phase estimates were determined using the SEM map of each sample. A wavelength dispersive Cameca SX-50 electron probe was used for quantitative analyses. The operating parameters were 15 kV accelerating voltage, 20 nA sample current, ca. 5 μm electron beam diameter and 10 s peak counting with 5 s background counting. The Cameca SX-50 was calibrated daily using natural and synthetic mineral standards. The detection limits for the major element oxides were approximately 0.02 wt.% and reproducibility was ± 0.30 wt.% or better [16].

2.3. Dissolution and ion-exchange chromatography

The remaining sub-sample was prepared for dissolution. Chondrules were cleaned of any adhering matrix by ultrasonic treatment in 18 MΩ water. Only the internal portions of CAIs, uncontaminated by iron rich matrix, were used for acid dissolution. Aristar® or UltraPur® grade acid and 18 MΩ deionised water were used throughout the procedure. All vessels used during sample preparation were leached using three stages of alternating 20% Aristar® HNO_3 and 18 MΩ

water at 120 °C for 5 h. Samples were digested in Teflon™ bombs using a two-stage dissolution method ($HF + HClO_4$ followed by HCl). Iron was quantitatively extracted from each sample by ion-exchange chromatography using Bio-Rad AG MP-1 anion exchange resin and HCl [1] in a method which does not differ significantly from that in use in other laboratories [e.g. [17–20]]. Samples were introduced to the pre-conditioned column in 7 M HCl and matrix elements were eluted with 7 M HCl (10 ml) followed by 6 M HCl (30 ml). Iron was eluted in 20 ml of 1 M HCl. To ensure elimination of Cl, each iron fraction was evaporated to dryness and taken up in 200 μl of 10% HNO_3 three times. After the last evaporation the sample was taken up in 2% HNO_3 in preparation for analysis. Iron fractions were assessed for purity prior to analysis using the MC-ICP-MS mass scan mode. In all cases the Fe-fractions did not contain any matrix elements. The pre- and post-iron recovery eluant was also analysed to ensure complete iron recovery. Thus, matrix elements were eliminated and iron was completely recovered during this one-pass column procedure. The integrity of the procedure was further examined by passing three aliquots of the IRMM-014 Fe-isotope standard doped with synthetic "matrix" elements through three separate ion-exchange columns. The isotopic composition of the processed IRMM-014 aliquots compared with untreated IRMM-014 were identical within ± 0.04‰ (2 SE).

2.4. Fe-isotope analysis

The ratios $^{56}Fe/^{54}Fe$ and $^{57}Fe/^{54}Fe$ were measured using a single focusing, fixed resolution ($m/\Delta m = 500$) IsoProbe™ MC-ICP-MS. Isobaric interferences from $^{14}N^{40}Ar^+$ ($m/z = 54$) and $^{16}O^{40}Ar^+$ ($m/z = 56$) were reduced to negligible levels by using a desolvating nebulizer and from collisions with argon gas within the hexapole collision cell [1]. However, $^{40}Ar^{16}O^1H^+$ ($m/z = 57$) was not eliminated by this method. The measurement precision on $m/z = 57$ ($^{57}Fe = 2.2\%$ abundance) improved with increased sample concentration. However, the intensity of the ion beam at $m/z = 56$ ($^{56}Fe = 91.5\%$ abundance) is a limiting factor on the concentration of the samples analysed. This problem was overcome by reducing the intensity of the ion beam for $m/z = 56$ by a factor of 10 by substituting the standard 10^{11} Ω resistor for a

10^{10} Ω resistor on the relevant Faraday collector [1]. In addition to polyatomic isobars, the ^{54}Cr isobar was also monitored. On-peak measurements for procedural blank solution were taken before each analysis. These blank contributions were negligible when compared with the absolute signal intensities. Precision was further enhanced by concentration matching standard and sample solutions to within 2%. As the concentration of iron in the samples was unknown, concentration matching was achieved by adding the solution to be analysed to the carrier acid in a stepwise manner using a linear regression until the analyte solution matched the concentration of the standard [1].

Fractionation was measured using the sample-standard bracketing (SSB) method [1] and quantified with respect to IRMM-014 using the delta notation (i.e., $\delta^{56}Fe_{IRMM}$ (‰) = ([$^{56}Fe/^{54}Fe_{sample}/^{56}Fe/^{54}Fe_{IRMM}$] − 1) × 1000). Each sample analysis included six to eight SSBs. Individual measurements consisted of (1) thirty 15 s on-peak integrations of a 2% HNO_3 blank, (2) 90 s washout with 4% HNO_3, (3) 120 s washout with 2% HNO_3, (4) thirty 15 s on-peak integrations of the analyte solution, (5) 120 s washout with 4% HNO_3 and (6) 120 s washout with 2% HNO_3. Prior to on-peak integrations (steps 1 and 4) the analyte solution (sample or standard) was allowed to condition for 90 s.

2.5. Precision and accuracy

Replicate analyses of each sample were obtained by splitting the digest into two or three equal parts and passing each split through the ion-exchange columns. These splits were measured during one or more analytical sessions. Analytical sessions were separated by days to months over a period of two years. Due to low iron content and/or low sample weights ALL-CAI-3, ALL-MTX-3 to 6 and CHP-MTX-2 were not split and with the exception of these samples the quoted Fe-isotope composition consists of a minimum of 24 individual SSBs. Errors are quoted at the 95% confidence interval and are calculated using the appropriate t-value (degree of freedom) for $\alpha = 0.05$, i.e. 2 SE. During the study period 69 repeated measurements, each consisting of six to eight SSBs, of IRMM-014 with respect to Johnson Matthey iron elemental standard solution gave the values $\delta^{56}Fe_{JM-Fe} = -0.54 \pm 0.03$‰ and $\delta^{57}Fe_{JM-Fe} = -0.80 \pm 0.04$‰ (2 SE).

3. Petrography of samples

3.1. Chondrules

Images of each chondrule are given in Fig. 1 and petrographical details are summarised in Table 1. The dominant chondrule textural type is porphyritic (Table 2, Fig. 1). Allende chondrules are dominated by type I compositions and the Chainpur chondrules consist of two type IIs and one type III (Table 2). Two chondrules (CHP-CL-1 and 3) contain glassy mesostasis (Table 3). The mesostasis of the remaining chondrules contain holocrystalline devitrification assemblages and of these chondrules, two show the effects of alkali ± halogen metasomatism (Table 2). All three porphyritic type I chondrules contain subhedral–anhedral enstatite adjacent to the chondrule rim (Tables 1 and 2, Fig. 1). Of these three chondrules, two contain large rounded opaques (ALL-CL-7 and 8) and one contains smaller irregular opaque inclusions (ALL-CL-5) (Table 2, Fig. 1).

3.2. Calcium–aluminium-rich inclusions (CAIs)

ALL-CAI-1 (Fig. 2a) is a fine-grained, zoned, oblong (longest axis=3.2 mm), spinel-rich inclusion with a concentric structure. Zone boundaries are gradational. The core (20 vol.%) contains fine-grained ($\leq$40 μm), anhedral nepheline (40 vol.%), spinel (40 vol.%), Al-diopside (<5 vol.%), and sodalite (15 vol.%). The middle zone (50 vol.%) is coarser grained ($\leq$70 μm) with similar composition to the core, but contains up to 20 vol.% Al-diopside and minor hedenbergite. The outer zone (30 vol.%) is 250 μm thick and contains fine-grained spinel (60 vol.%), sodalite (20 vol.%), nepheline (20 vol.%), and Al-diopside (<1 vol.%).

ALL-CAI-2 (Fig. 2b) is a 2.8 mm long, irregularly shaped, concentrically zoned object with indistinct boundaries. The core (85 vol.%) contains 40 vol.% anhedral spinel (~15 wt.% FeO) nodules (10–50 μm) with porous rims (<5 μm thick) consisting of anorthite and diopside. The inter-nodule groundmass contains fine-grained nepheline (35 vol.%), hedenbergite–augite (20 vol.%), andradite (5 vol.%) and rare sodalite and clintonite (<1 vol.% combined). The middle zone is similar in composition to the core, but with smaller grain sizes, and this zone is rimmed with fine-grained material approximately 100 μm thick.

ALL-CAI-3 (Fig. 2c) is an irregularly shaped (max. 4 mm long) inclusion with four concentric zones from core (zone A) through to the outer rim (zone D). *Zone A* contains closely packed, anhedral, zoned spinel nodules (<10–70 μm), interspersed with Al–Ti diopside-rimmed vuggy cavities and fine-grained angular spinel. Spinels are rimmed and the typical rim sequence (from centre to edge) is clintonite (10 μm), Al–Ti-diopside (5 μm), hedenbergite or spinel (5 μm), anorthite (10 μm), Al–Ti-diopside (10 μm). *Zone B* (0.4 to 1.4 mm thick) is dominated by a heterogeneous mixture of gehlinitic melilite and spinel with rare hedenbergite. Al–Ti diopside rimmed vugs are less common than in zone A. *Zone C* ($\leq$100 μm thick) is a continuous rim of spinel with <10 vol.% melilite and rare, small (<50 μm) Al–Ti-diopside rimmed vugs. *Zone D* (100–300 μm thick) contains closely packed, fine-grained (<10 μm) melilite with Al–Ti-diopside and minor spinel and this zone is clearly distinct from the host matrix.

3.3. Allende matrix

The sections of Allende matrix studied here contain dominantly fine-grained (<10 μm) platy forsteritic olivine (Fo_{47-54}). Minor silicate phases (<5 vol.%) are fine-grained (<10 μm) pyroxene (En_{73-96} $Fs_{1-5}Wo_{1-25}$) and trace (<0.5 vol.%) nepheline. Amoeboid olivine aggregates (<100 μm) and dark inclusions (<150 μm) are embedded in this matrix. The opaque assemblage (<5 vol.%) is dominated by pentlandite which occurs as (1) isolated grains ($\leq$10 μm), (2) altered, fine-grained irregular aggregates ($\leq$75 μm), (3) rounded, altered oblong grains (most common) or (4) more coarse-grained (80–150 μm) rounded or irregular nuggets. Awaruite (1.8 to 1.9 wt.% Co) and troilite are minor opaque phases. Based on the composition and modes of the constituent components and minerals, the bulk FeO content of Allende is 29 wt.% and the bulk FeO content of the matrix is 35 wt.%, which agrees well with previous detailed work [21].

4. Fe-isotope systematics of samples

Iron isotope compositions (Table 4) are plotted as $\delta^{56}Fe_{IRMM}$ and $\delta^{57}Fe_{IRMM}$ on a three-isotope dia-
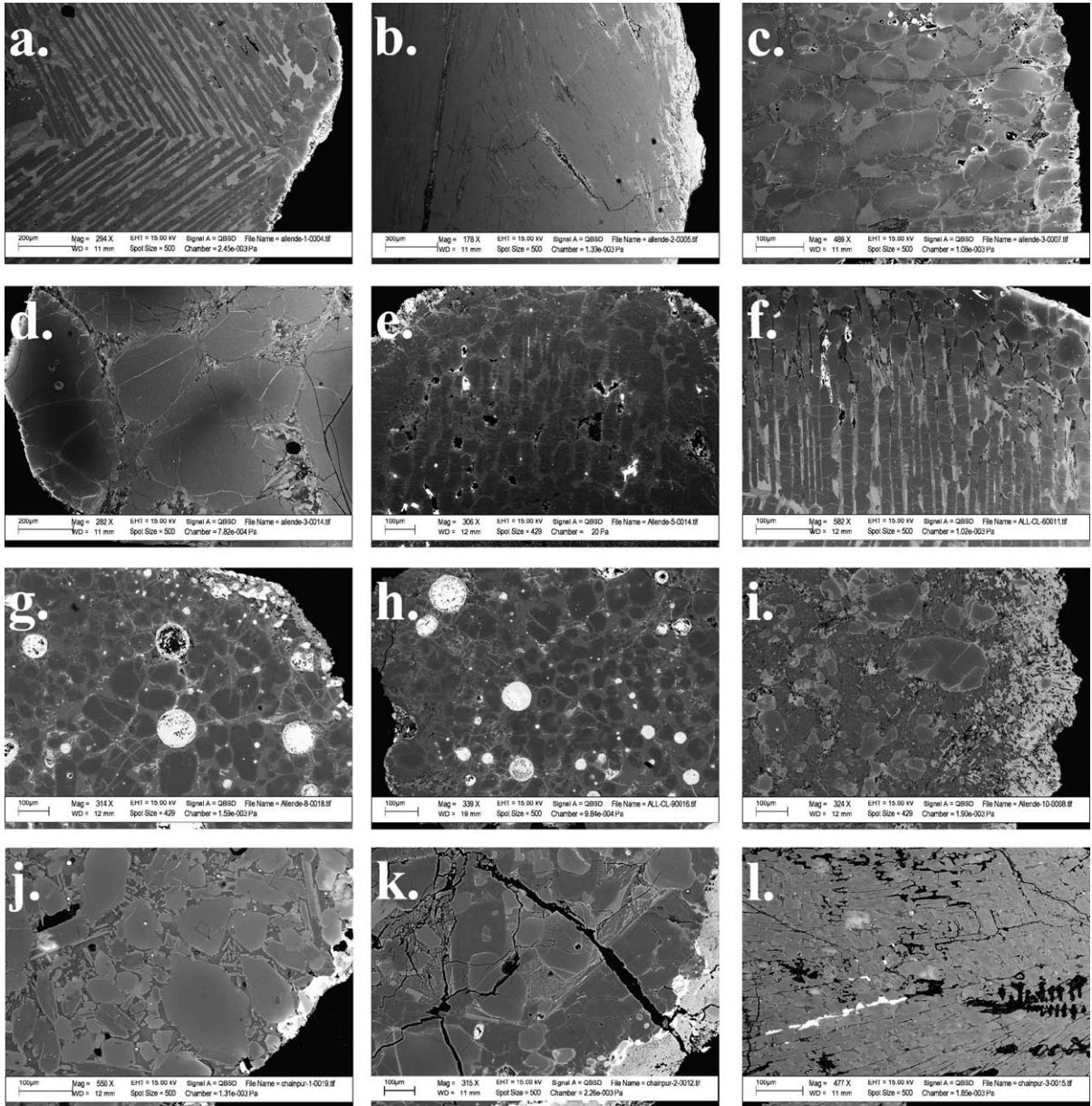
Fig. 1. Back scattered electron images of (a) ALL-CL-1 type I barred olivine chondrule, (b) ALL-CL-2 type III radial pyroxene chondrule, (c) ALL-CL-3 type II porphyritic olivine chondrule, (d) ALL-CL-4 type II porphyritic olivine chondrule, (e) ALL-CL-5 type I porphyritic olivine chondrule, (f) ALL-CL-6 type I barred olivine chondrule, (g) ALL-CL-7 type I porphyritic olivine chondrule, (h) ALL-CL-8 type I porphyritic olivine chondrule, (i) ALL-CL-9 type II porphyritic pyroxene olivine chondrule, (j) CHP-CL-1 type II porphyritic olivine pyroxene chondrule, (k) CHP-CL-2 type II porphyritic pyroxene olivine chondrule and (l) CHP-CL-3 type III radial pyroxene chondrule. See Tables 1 and 2 for petrographical details.

gram (Fig. 3). Iron isotope compositions are all consistent with mass-fractionation of a single isotopically homogeneous source. No mass-independent isotope anomalies have been found. The chondrule mass-fractionation line is defined by the equation $\delta^{57}Fe_{IRMM} = (1.45 \pm 0.05) \cdot \delta^{56}Fe_{IRMM} - (0.01 \pm 0.02)$

Table 1
Petrographical properties of each chondrule sample

A. Type 1 barred olivine (BO) chondrules

	Olivine Bars	Mesostasis	Rim	Accessory phases
ALL-CL-1 (Fig. 1a)	Fo_{88-97}, unzoned, 20 μm thick.	Plagioclase laths (An_{91-97}) set in diopside ($En_{50-59}Fs_{3-5}Wo_{36-47}$).	Olivine, Fo_{85}.	Chromite (3 vol.%).
ALL-CL-6 (Fig. 1f)	Fo_{90-94}, unzoned, 5 to 20 μm thick.	Fine grained (≤20 μm) diopside ($En_{41-52}Fs_{5-7}Wo_{41-54}$).	Inner rim diopside (≤30 μm), partial outer rim of opaques (5 μm).	<1 vol.% opaques (troilite and pentlandite) in mesostasis.

B. Type III radial pyroxene (RP) chondrules

	Enstatite	Mesostasis	Rim	Accessory phases
ALL-CL-2 (Fig. 1b)	100 vol.%, $En_{86-93}Fs_5Wo_{2-9}$.	None.	Olivine, Fo_{60-78}, 100–150 μm thick.	None.
CHP-CL-3 (Fig. 1l)	97 vol.%, skeletal, $En_{82-90}Fs_{10-15}Wo_3$.	Glassy, 3 vol.%.	None.	<0.1 vol.% opaques (<2 μm) scattered evenly in mesostasis, 15×300 μm vein of troilite+minor kamacite.

C. Type I and II porphyritic chondrules

	Phenocryst phase(s)	Mesostasis	Accessory opaques and rim
ALL-CL-3 PO (Fig. 1c)	Dominant phase: olivine, subhedral, ≤150 μm long, cores=Fo_{82-86}, rims=Fo_{86-92}, <40 μm phenocrysts=Fo_{86-88}. Subordinate phase: Rare Al–Ti-diopside, ≤50 μm, anhedral, $En_{50-64}Fs_{4-5}Wo_{31-46}$.	An_{89-95}, minor diopside (avg. $En_{50}Fs_5Wo_{45}$).	Opaques: round, ≤5 μm in size, ≤1 vol.%, occur in mesostasis and enclosed within olivine. Rim: none.
ALL-CL-4 PO (Fig. 1d)	Olivine, ≤600 μm, euhedral, cores=Fo_{94-99}, rims=Fo_{89-93}.	$An_{77 \pm 1.4}$–pyroxene ($En_{50-74}Fs_{14-17}Wo_{9-36}$) intergrowth.	Opaques: none. Rim: none.
ALL-CL-5 PO (Fig. 1e)	Olivine, ≤220 μm, zoned (Fo_{83-99}). Some cores contain fayalitic olivine.	An_{78-97} with minor, ≤50 μm, diopside and enstatite ($En_{88 \pm 2}Fs_{5 \pm 1}Wo_{6 \pm 1}$).	Opaques: <1 vol.% troilite+minor pentlandite blebs (5–30 μm) and stringers (≤100 μm) in mesostasis. Rim: enstatite, discontinuous, with fine-grained opaques on the outermost margin.
ALL-CL-7 PO (Fig. 1g)	Olivine, 75 vol.%. 30–160 μm are weakly zoned (Fo_{91-96}). ≤30 μm are heterogeneous (Fo_{88-94}) and unzoned.	Plagioclase ($An_{89 \pm 1}$), rare diopside (avg.$En_{46}Fs_5Wo_{49}$) and ferroan spinel (FeO=4–13 wt.%), ≤20 vol.%, locally altered to nepheline.	Opaques: spherical-ovoid inclusions (≤5–200 μm), 5 vol.%, pentlandite, troilite or magnetite–awaruite. Also as rare, fine-grained (<5 μm) inclusions in olivine. Rim: enstatite, ≤20 μm thick, average $En_{92}Fs_3Wo_5$ with minor fine-grained (<5 μm) opaques.
ALL-CL-8 PO (Fig. 1h)	Olivine, subhedral-rounded, weakly zoned ($Fo_{95-96.5}$). Smaller olivines are more fayalitic. One relict type II olivine core.	An_{78-95} with ≤10 μm diopsides ($En_{49}Fs_4Wo_{47}$).	Opaques: round (≤180 μm) inclusions, 5 vol.%, pentlandite, minor magnetite, awaruite and troilite intergrowths. Also as ≤10 μm inclusions in olivine. Rim: enstatite (≤Wo_{10}), discontinuous, max. ≤20 μm thick, sometimes encloses olivine phenocrysts.

Table 1 (*continued*)

C. Type I and II porphyritic chondrules

	Phenocryst phase(s)	Mesostasis	Accessory opaques and rim
ALL-CL-9 PPO (Fig. 1i)	Dominant phase: enstatite, ($En_{94–95}Fs_{2–4}Wo_2$), <50 to 250 μm, 80 vol.%, sometimes enclose olivine phenocrysts. Subordinate phase: olivine, $Fo_{74–98}$, 15 vol.%, subhedral–anhedral, <10 to 350 μm. Larger olivines strongly zoned ($Fo_{96–80}$). Smaller more fayalitic olivines are unzoned.	5 vol.%, fine grained (≤30 μm), Sodalite and anhedral diopside ($En_{50–54}Fs_2Wo_{44–48}$).	Opaques: none. Rim: enstatite+ fayalitic olivine+minor fine-grained diopside (<20 μm)+pentlandite (<30 μm), irregular, ≤150 μm thick.
CHP-CL-1 POP (Fig. 1j)	Dominant phase: olivine, 65 vol.%, mainly euhedral. Larger olivines are strongly zoned ($Fo_{74–93}$). Smaller olivines ($Fo_{75–84}$) are unzoned. Subordinate phase: enstatite, avg. $En_{81}Fs_{17}Wo_2$, ≤250 μm, with rim (<15 μm) of diopside (avg. $En_{44}Fs_{18}Wo_{38}$).	Mainly glassy, some ≤10 μm skeletal diopside (avg. $En_{41}Fs_{20}Wo_{39}$).	Opaques: some ~30 μm rounded opaques in mesostasis. Rim: thin (<25 μm), discontinuous, troilite (~50 μm) with minor kamacite, awaruite and phosphate.
CHP-CL-2 PPO (Fig. 1k)	Dominant phase: enstatite, $En_{90–95}Fs_{4–9}Wo_{0.5}$, anhedral, 80 vol.%, up to 150 μm long. Subordinate phase: olivine, 15 vol.%, 70–120 μm size are zoned ($Fo_{92–97}$), ~50 μm size are unzoned (Fo_{76}).	5 vol.%, Average An_{88}.	Opaques: <10 μm grains in mesostasis. One round inclusion (80 μm diameter) of troilite+kamacite. Rim: inner rim of enstatite ($En_{88–90}Fs_{9–11}Wo_1$), middle rim ≤5 μm thick of troilite, outer rim of ≤50 μm fine-grained olivine ($Fo_{31–38}$).

with R^2=0.9995 (Fig. 3a). The Allende bulk composition is $\delta^{56}Fe_{IRMM}$=−0.05 ± 0.05‰ (Table 4).

The average composition of Allende interchondrule matrix ($\delta^{56}Fe_{IRMM}$=−0.07 ± 0.02‰, n=6) is similar to that of bulk Allende ($\delta^{56}Fe_{IRMM}$=−0.05 ± 0.05‰) (Fig. 3b). To examine whether Fe-isotopes were heterogeneously distributed within the matrix a number of smaller aliquots of approximately 1 mg were taken from Allende matrix (ALL-MTX-3 to 6). The isotopic compositions of these aliquots were similar to ALL-MTX-1 and 2 indicating relative homogeneity on the scale of 1 mg.

The Fe-isotope compositions of ALL-CAI-1 (7.5 wt.% bulk FeO) and ALL-CAI-2 (11.8 wt.% bulk FeO) are similar to the composition of the host matrix and bulk Allende composition, but the Fe-isotope composition of ALL-CAI-3 (0.4 wt.% bulk FeO) is lighter than the matrix by up to 0.11‰ for $\delta^{56}Fe$ (Fig. 3b).

Allende chondrules show a greater range of fractionation, from $\delta^{56}Fe_{IRMM}$=−1.33‰ (ALL-CL-3) to +0.65‰ (ALL-CL-1) than Chainpur chondrules ($\delta^{56}Fe_{IRMM}$=−0.18 to +0.27‰) (Fig. 3a). The

reduced range of isotope composition within Chainpur chondrules may be due to the smaller sample set. Many of the chondrules are isotopically distinct from their host interchondrule matrix (Table 4). The extent of fractionation of chondrules appears to be size related, with larger chondrules more fractionated (with respect to bulk Allende) than smaller chondrules, although this relationship is complicated, with larger chondrules being both isotopically heavy and light (Fig. 4). The Fe-isotope compositions of type I and II chondrules (with the exception of CHP-CL-2 and type III chondrules) are negatively correlated with bulk FeO content (Fig. 5).

5. Discussion

Although very rare mass-independent fractionation of ^{58}Fe has been found in FUN inclusions from Allende [12], iron isotope signatures indicative of mass-independent fractionation are not observed here and this concurs with previous studies [5–7]. In the following discussion we explore the reasons for

Table 2
Physical and chemical properties of chondrule samples

Meteorite	Allende (ALL-CL-)									Chainpur (CHP-CL-)		
Chondrule number	1	2	3	4	5	6	7	8	9	1	2	3
Textural type[a]	BO	RP	PO	PO	PO	BO	PO	PO	PPO	POP	PPO	RP
Compositional type[b]	I	III	II	II	I	I	I	I	II	II	II	III
Diameter (mm)[c]	2.0	2.1	2.2	1.2	1.6	1.4	1.2	1.1	1.7	1.3	1.6	1.5
Shape[d]	S	O	S	O	S	S	S	I	S	S	S	S
Glassy mesostasis										✔		✔
Devitrified with plagioclase and pyroxene	✔		✔	✔	✔	✔	✔	✔			✔[e]	
Clinoenstatite on outer margin					✔		✔	✔			✔	
Radial pyroxene with no mesostasis		✔										
Alkali metasomatism							✔		✔			
Halogen metasomatism									✔			
Rounded opaques (up to 200 μm in diameter)[f]	MP	MP	MP	MP	✔	MP	✔	✔	MP	MP	MP	–
Zoning in olivine phenocrysts[g]	NZ	–	5[h]	11	3	NZ	3	2	16	2	5	–

[a] Chondrule textural types are: barred olivine (BO); radial pyroxene (RP); porphyritic olivine (PO); porphyritic pyroxene olivine (PPO) and porphyritic olivine pyroxene (POP).
[b] Chondrule compositional types are: type I — FeO poor with olivine composition of Fo_{90-100}; type 2 — FeO rich with Fo_{50-85}; type III — radial pyroxene chondrules.
[c] Diameter: is the true chondrule diameter which was measured prior splitting.
[d] Chondrule shapes are spherical (S), oblong (O), or irregular (I).
[e] Mesostasis contains only anorthitic plagioclase.
[f] MP indicates metal poor chondrules.
[g] Average variation in mole percent Fo from core to rim within zoned olivine phenocrysts, NZ indicates that the olivine phenocrysts are not zoned.
[h] Olivine phenocrysts in this chondrule contain fayalitic cores and forsteritic rims.

Fe-isotope fractionation following homogenization of the Fe-isotope reservoir.

5.1. Bulk and matrix Fe-isotope composition

It was long believed that type 3 chondrites contain a pristine matrix, but it is now accepted that many type 3 matrices contain a strong imprint of aqueous alteration [e.g. [22]]. The matrix within our Allende sections is dominated by fayalitic olivine with minor contributions from other phases. Thus, fayalitic olivine is the dominant iron carrier. There are two models for the origin of fayalitic olivine in CV3 chondrites. The vaporization/recondensation

Table 3
Major element oxide (wt.%) composition of glassy mesostasis from CHP-CL-1 and 3

	CHP-CL-1			CHP-CL-3		
	Min.	Max.	Average ± 2 SE	Min.	Max.	Average ± 2 SE
Na_2O	0.59	6.25	2.51 ± 0.42	0.28	3.53	2.21 ± 0.78
MgO	0.72	4.95	2.60 ± 0.39	0.58	2.20	10.3 ± 0.38
Al_2O_3	9.97	14.35	11.97 ± 0.33	16.12	17.56	17.20 ± 0.36
SiO_2	68.20	78.76	73.36 ± 0.99	70.71	75.90	73.92 ± 1.50
K_2O	0.01	1.75	1.24 ± 0.18	0.66	1.87	1.47 ± 0.26
CaO	0.09	6.65	3.07 ± 0.61	0.09	1.13	0.33 ± 0.26
P_2O_5	0.01	0.15	0.08 ± 0.01	0.00	0.03	0.01 ± 0.01
TiO_2	0.37	0.61	0.49 ± 0.02	0.33	0.56	0.46 ± 0.05
Cr_2O_3	0.01	0.37	0.08 ± 0.02	0.00	0.12	0.04 ± 0.03
MnO	0.01	0.21	0.10 ± 0.02	0.00	0.08	0.04 ± 0.02
FeO	1.46	8.12	3.19 ± 0.52	1.12	1.53	1.31 ± 0.10

Analyses obtained using a Cameca SX-50 wavelength dispersive electron probe. 2 SE error based on 156 values for CHP-CL-1 and 43 analyses for CHP-CL-3.
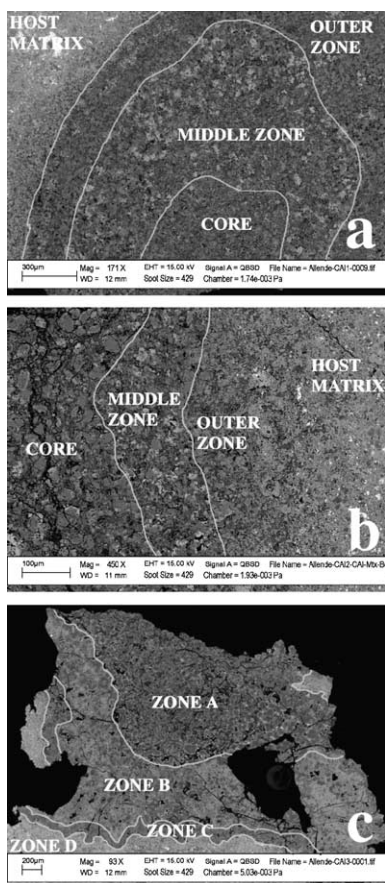
Fig. 2. Back scattered electron images of (a) ALL-CAI-1, (b) ALL-CAI-2, and (c) ALL-CAI-3 which are all fine-grained, spinel rich, Ca–Al-inclusions. See text for detailed petrographical descriptions.

model [23] advocates formation of fayalitic olivine in the nebula. In contrast, the hydration/dehydration model [15,24] proposes that fayalitic olivine is an end-product of complex secondary processing during parent body residence. Compositional variation within CV matrix olivine has been used to estimate the degree of equilibration of individual members of the CV group and within this scheme matrix from Allende is moderately equilibrated [e.g. [15,22]].

The average $\delta^{56}Fe_{IRMM}$ value for Allende matrix, based on six separate matrix aliquots, is $-0.07 \pm 0.02‰$ and the average $\delta^{56}Fe_{IRMM}$ value for Chainpur matrix, based on two separate matrix aliquots is $-0.01 \pm 0.03‰$ (Table 4). The average matrix value for both chondrites lies close to the bulk Allende composition ($\delta^{56}Fe_{IRMM} = -0.05‰$). These relatively

homogeneous compositions may be the result of parent body hydration/dehydration as significant fluid migration could extensively homogenize the Fe-isotope signatures. However, previously published $\delta^{56}Fe_{IRMM}$ values for Allende matrix are $+0.09 \pm 0.06‰$ (2 SD) [5] and $-0.06 \pm 0.01‰$ (2 SD) [7]. Thus, the Fe-isotope composition of Allende matrix may be more heterogeneous than the results of this study indicate. A $\delta^{56}Fe_{IRMM}$ value of $+0.43 \pm 0.06‰$ was previously quoted for Chainpur matrix [5], which is significantly different to the values obtained for the two aliquots measured here. This indicates that the isotopic composition of Chainpur matrix may also be heterogeneous.

5.2. Fe-isotope composition of CAIs

No previous measurements of Fe-isotopes ($\delta^{56}Fe$ and $\delta^{57}Fe$) in CAIs have been reported, although the ratios $^{57}Fe/^{56}Fe$ and $^{58}Fe/^{56}Fe$ were reported in FUN inclusions from Allende [12]. CAIs were only recovered from Allende. These objects are all concentrically zoned, fine-grained, spinel-rich inclusions (FGI) (Fig. 2). Spinel-rich FGIs are thought to be aggregates of independently formed grains [e.g. [25]]. The compositions of Allende FGIs are believed to be heavily modified by the effects of Fe–alkali–halogen metasomatism and several of the phases (e.g. andradite, hedenbergite and nepheline) are secondary; many developed at the expense of melilite [[26] and references therein]. FGI from reduced CV3s (e.g. Leoville and Efremovka) are considered to be less altered than those from Allende and, consequently, may represent pre-metasomatic chemical compositions [27]. The average bulk FeO composition of twelve FGIs from Leoville and Efremovka is 1.3 wt.% [calculated from data given in Krot et al. [27]], which is significantly less than the bulk FeO content of ALL-CAI-1 and 2 (>7 wt.%). In contrast, ALL-CAI-3 only contains 0.4 wt.% bulk FeO (Table 4) and is the only FGI to contain the primary mineral melilite. This suggests that ALL-CAI-1 and 2 have been subject to more extensive iron metasomatism than ALL-CAI-3.

The location of Fe–alkali–halogen metasomatism, whether nebular or asteroidal, is debated [15]. If metasomatism occurred in the nebula then iron was introduced by condensation onto FGI surfaces. Alternatively, if metasomatism occurred on the parent body

Table 4

Iron isotope composition for chondrules, CAIs and matrix from Allende CV3 (BM 1969,148) and Chainpur LL3 (BM 1915,86) chondrites

Sample	Type[a]	Weight (mg)[b]	Bulk FeO (wt.%)[c]	No. of replicates[d]	$\delta^{56}Fe_{IRMM}$ (‰)[e]	$\pm$ 2 SE[f]	$\delta^{57}Fe_{IRMM}$ (‰)[e]	$\pm$ 2 SE[f]
Allende Bulk	–	2800	29.0	6	−0.05	0.05	−0.08	0.06
ALL-CL-1	BO, I	56	6.5	4	+0.65	0.04	+0.93	0.05
ALL-CL-2	RP, III	69	7.5	5	−0.69	0.03	−1.06	0.06
ALL-CL-3	PO, II	64	11.5	4	−1.33	0.04	−1.96	0.06
ALL-CL-4	PO, II	13	7.6	4	−0.03	0.04	−0.03	0.05
ALL-CL-5	PO, I	32	6.6	5	+0.34	0.05	+0.46	0.07
ALL-CL-6	BO, I	22	6.7	3	+0.16	0.04	+0.20	0.07
ALL-CL-7	PO, I	19	7.8	4	−0.09	0.06	−0.02	0.07
ALL-CL-8	PO, I	14	7.0	4	−0.05	0.05	−0.03	0.06
ALL-CL-9	PPO, II	49	10.0	5	−0.36	0.04	−0.42	0.07
ALL-CAI-1	FGSR	178	7.5	4	−0.03	0.07	−0.06	0.09
ALL-CAI-2	FGSR	239	11.8	4	−0.08	0.05	−0.10	0.07
ALL-CAI-3	FGSR	315	0.4	2	−0.16	0.06	−0.29	0.08
ALL-MTX-1	Matrix	82	–	4	−0.04	0.04	−0.06	0.06
ALL-MTX-2	Matrix	96	–	4	−0.07	0.04	−0.08	0.05
ALL-MTX-3	Matrix	1.2	–	3	−0.05	0.03	−0.07	0.05
ALL-MTX-4	Matrix	0.8	–	3	−0.10	0.06	−0.14	0.07
ALL-MTX-5	Matrix	1.1	–	2	−0.08	0.05	−0.13	0.04
ALL-MTX-6	Matrix	1.2	–	3	−0.05	0.05	−0.06	0.05
Average ($n=6$)[g]	Matrix				−0.07	0.02	−0.09	0.03
CHP-CL-1	POP, II	22	8.7	4	−0.18	0.05	−0.22	0.06
CHP-CL-2	PPO, II	39	9.3	5	+0.20	0.06	+0.25	0.06
CHP-CL-3	RP, III	28	6.9	4	+0.27	0.07	+0.40	0.07
CHP-MTX-1	Matrix	55	–	4	+0.02	0.03	+0.04	0.06
CHP-MTX-2	Matrix	11	–	3	−0.03	0.05	−0.01	0.07
Average ($n=2$)[g]	Matrix				−0.01	0.03	+0.02	0.03

[a] Sample type (see caption for Table 2).
[b] The sample weight given is the amount digested for isotopic analysis.
[c] Bulk FeO is calculated on the basis of FeO content and the modes of the constituent minerals.
[d] Each replicate consists of 6 to 8 SSBs.
[e] $\delta^{56}Fe$ and $\delta^{57}Fe$ are quoted with respect to the IRMM-014 Fe-isotope standard.
[f] The error quoted is the 95% confidence interval (2 SE).
[g] Average Fe-isotope composition of the matrix aliquots.

then iron most likely derives from matrix components [28]. The $\delta^{56}Fe_{IRMM}$ composition of ALL-CAI-1 (−0.03‰) and ALL-CAI-2 (−0.08‰) are similar to that of the average host matrix (−0.07‰) and bulk Allende (−0.05‰) compositions. These similarities suggest that Fe-metasomatism occurred largely during parent body residence and the more severely metasomatized FGI have fully equilibrated with bulk/matrix Fe-isotope compositions. However, further analyses of FGI samples would be needed to fully substantiate this, and as a result nebular metasomatism cannot be precluded.

The $\delta^{56}Fe_{IRMM}$ composition of ALL-CAI-3 (−0.16‰, 0.4 wt.% FeO) is significantly different to the bulk FeO-rich FGI. It is possible that the iron contained within ALL-CAI-3 is 'primary', i.e. captured during condensation of the primary phases in the cooling solar nebula. If this is the case then this condensed iron could be expected to be isotopically heavy relative to bulk Allende, assuming that the heavier isotopes of iron are preferentially condensed. However, this is not what we observe. The isotopically light signature of this CAI may be explained by condensation of iron from a gas from which material with isotopically heavier iron had already condensed. ALL-CAI-3 may have escaped the relatively pervasive parent body metasomatism due to its morphology. The outermost zones of ALL-CAI-1 (Fig. 2a) and ALL-CAI-2 (Fig. 2b) are porous and are clearly gradational with the host matrix. In contrast, the two
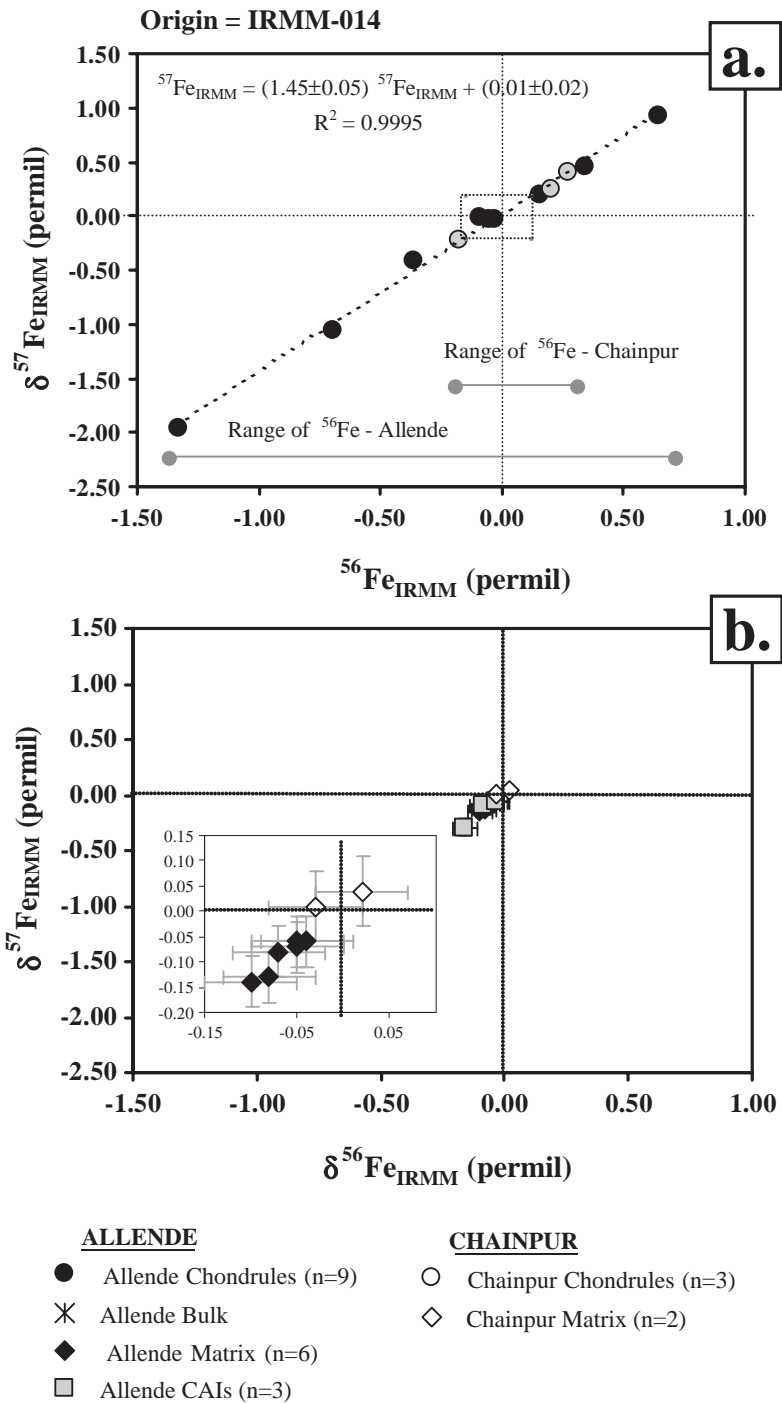
Fig. 3. Plots of $\delta^{56}Fe_{IRMM}$ (‰) vs. $\delta^{57}Fe_{IRMM}$ (‰). The origin represents the composition of the IRMM-014 standard. (a) Allende chondrules, Chainpur chondrules and bulk Allende. The equation of the mass-fractionation line defined by chondrule Fe-isotope compositions is also included. Error bars are smaller than the symbols used. (b) Allende CAIs, Allende matrix and Chainpur matrix. The boxed area is and enlarged view of matrix Fe-isotope signatures.
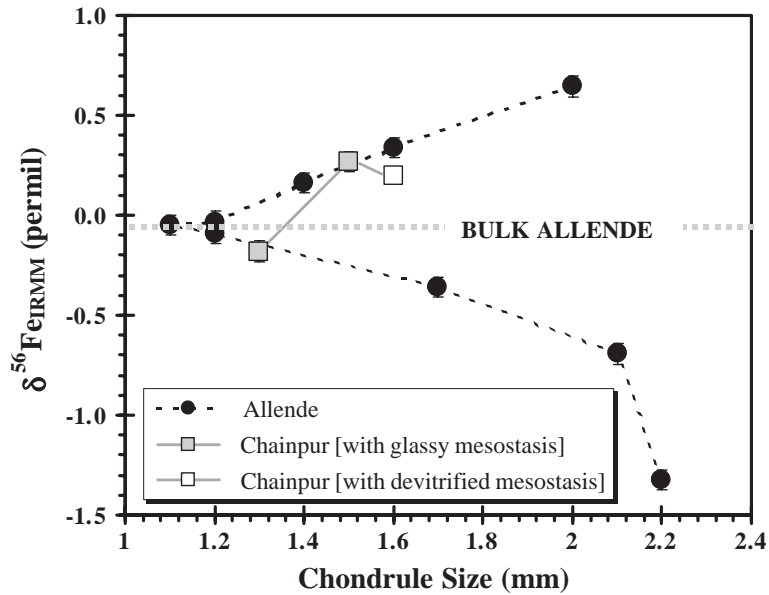
Fig. 4. $\delta^{56}Fe_{IRMM}$ of Allende chondrules compared with their true size (mm). The $\delta^{56}Fe_{IRMM}$ composition of bulk Allende is indicated by the dashed line. Error bars for $\delta^{56}Fe_{IRMM}$ are mainly smaller than the symbols used.

outermost zones (C and D) of ALL-CAI-3 are continuous, relatively compact and clearly distinct from the matrix (Fig. 2c). These zones may have acted as an impenetrable barrier which shielded this FGI from the effects of metasomatism. Alternatively, the iron may have been incorporated during metasomatism, in which case this process may preferentially mobilise the lighter isotopes of iron.
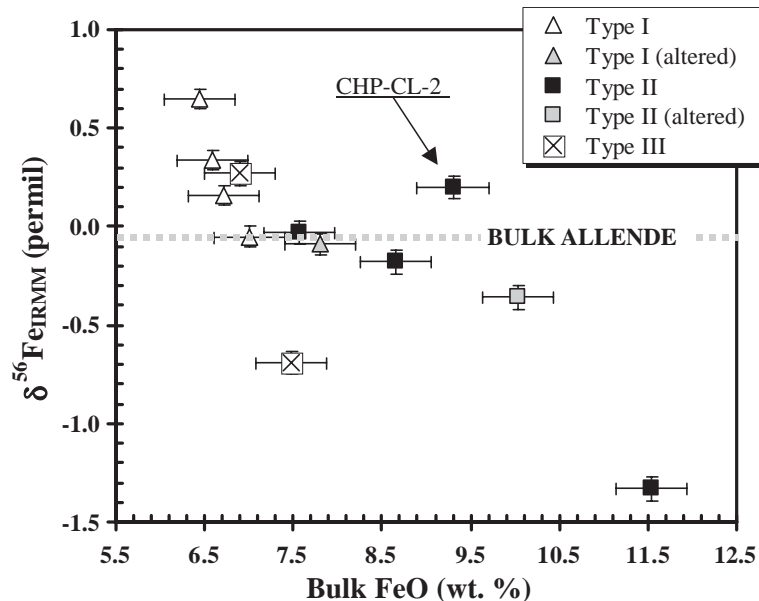

Fig. 5. Bulk FeO (wt.%) content of each chondrule (classified by compositional type) vs. $\delta^{56}Fe_{IRMM}$. Bulk FeO contents are calculated from EMP data and the error on these calculations is estimated to be ± 0.5 wt.%.

5.3. Fe-isotope composition of chondrules

Most chondrules are isotopically distinct from the matrix. Fe-isotope fractionation extends in both isotopically light and heavy directions with respect to the bulk composition of Allende. We observe a greater range of Fe-isotope fractionation ($-1.33 \leq \delta^{56}Fe_{IRMM} \leq +0.65$‰, Fig. 3a) than has been previously documented, e.g. $-0.88 \leq \delta^{56}Fe_{IRMM} \leq +0.93$‰, for seven chondrules (5 from Allende and 2 from Chainpur) [5] and $-0.45 \leq \delta^{56}Fe_{Kil1919} \leq 0.00$ for eight chondrules from Tieschitz (H3.6).

The currently favoured hypothesis for chondrule formation is by melting of precursor material in the solar nebula by multiple, localised, transient, high-temperature melting episodes [29]. The Fe-isotope composition of chondrules could have been inherited from the precursor material. However, it is likely that the precursor composition has been modified by subsequent processing such as evaporation or metasomatism. As the effects of metasomatism, in some cases, will have overprinted the fractionation effects produced during chondrule melting we first evaluate our data with respect to metasomatism.

5.3.1. Metasomatism

The chondrules in this sample set show a variety of alteration effects, i.e. devitrification of mesostasis, formation of enstatite rims (indicating gas–melt interactions) and alkali-, halogen-metasomatism (Table 2). Smaller Allende chondrules are less fractionated than larger chondrules (Fig. 4) suggesting that smaller chondrules are more susceptible to metasomatic exchange and that exchange drives isotopic compositions towards bulk- or matrix-like values. The size-fractionation trend for Chainpur chondrules is not as systematic (Fig. 4). This less systematic behaviour may either be a function of the alteration history of these chondrules or it may simply be due to the smaller sample set. If the absence of glassy mesostasis is taken as an indicator of chondrule alteration then the Allende chondrules, all of which lack glassy mesostasis, are altered to some degree. Both CHP-CL-1 and 3 (grey squares, Fig. 4) contain glassy mesostases. CHP-CL-2 (white square, Fig. 4) contains devitrified mesostasis and thus the isotopic signature of this chondrule may have been modified during alteration. If devitrification is accompanied by iron metasomatism, where iron is derived from the matrix, then the Fe-isotope composition of CHP-CL-2 would be less fractionated in composition when compared to an unaltered chondrule of comparable size, which is what we observe in Fig. 4.

The most extreme mesostasis alteration is seen in ALL-CL-9, which contains sodalite and nepheline. The presence of these minerals indicates significant introduction of Na_2O and Cl during alkali-, halogen-metasomatism. It is not clear to what extent iron was introduced during metasomatism. ALL-CL-9 is not the least fractionated of the Allende chondrules. For example, ALL-CL-4, which has only been devitrified is less fractionated. However, ALL-CL-4 is smaller than ALL-CL-9, suggesting that chondrule size is an important factor.

The presence of enstatite adjacent to chondrule margins indicates that gas–melt interactions occurred in the nebula [23]. All porphyritic type I chondrules examined here (ALL-CL-5, 7 and 8) contain a discontinuous, coarse-grained, subhedral–anhedral mantle of low-Ca pyroxene adjacent to the chondrule margin. Low-Ca pyroxene crystallizes only in melts with high Si activity and peripheral enstatite may arise by gas–melt interactions through condensation of $SiO_{(g)}$ onto the chondrule surface [30]. High $SiO_{(g)}$ partial pressure may have been produced by volatilisation in areas of the nebula with a high dust/gas ratio [30]. ALL-CL-7 and 8 contain more extensive enstatite mantles than ALL-CL-5; possibly indicating enhanced back-reaction of ALL-CL-7 and 8 with the nebular gas. If exchange with nebular gas includes iron in addition to silicon then enhanced back-reaction could reduce the Fe-isotope fractionation produced by evaporation. This hypothesis is supported by our data as ALL-CL-7 and 8 are among the least fractionated chondrules. Recondensation of evaporated material has previously been suggested in order to explain the lack of K- [31] and Fe-isotope [14] fractionation. In summary, it is likely that the Fe-isotope composition of these chondrules has been metasomatically modified and the resulting Fe-isotope signature is a product of interplay between chondrule size, degree of metasomatic alteration and back-reaction with the nebular gas.

5.3.2. Chondrule melting events

Chondrules require high-temperature melting events of relatively short duration (minutes) to explain their textural characteristics [29]. Iron isotope fractio-

nation does not vary systematically with chondrule texture. Chondrules that experienced almost complete melting (barred olivine and radial pyroxene chondrules) are both isotopically light (ALL-CL-2) and heavy (ALL-CL-1 and 6, and CHP-CL-3) with respect to bulk Allende (Table 4). Therefore, it is clear that the most recent melting event did not dictate the Fe-isotope composition of these chondrules. Many chondrules may have been melted more than once, and chondrule compositional diversity may be due to repeated melting [e.g. [32]] with each melting episode vaporising successively more iron and silicon. Isotopically heavier chondrules may be the product of repeated melting whereas isotopically lighter chondrules may be less reworked. Type II chondrules are less refractory [e.g. [33]] and more volatile-rich [e.g. [34]] than type I chondrules. These characteristics suggest that type I chondrules (FeO-poor) were derived by volatilisation of silicon and iron from type II chondrules (FeO-rich) [e.g. [35]]. If this theory is valid then type I chondrules should be isotopically heavier than type II chondrules. When Fe-isotope compositions are plotted against bulk FeO content (Fig. 5) it is evident that type I chondrules are mainly isotopically heavier than type II chondrules, although CHP-CL-2 lies off this trend. The reason why CHP-CL-2 is different may be due to its unusual devitrified mesostasis composition. All of the other chondrules which contain devitrified mesostases contain iron-bearing pyroxene in addition to plagioclase, but CHP-CL-2 only contains plagioclase (Tables 1c and 2). Leaching of iron during devitrification may have produced the anomalously heavy Fe-isotope composition within CHP-CL-2. Thus, with the exception of CHP-CL-2, Fe-isotope compositions appear to be related to bulk chondrule chemistry and these data support the theory that type I chondrules are the product of evaporative loss of iron and silicon from type II chondrules. Previously, Alexander and Wang [14] examined the same theory using Fe-isotopes measured by ion probe. Their data did not support the evaporation hypothesis. However, the precision obtainable by ion probe ($\pm 2‰$/amu) is greater than the small fractionation effects present within chondrules.

Radial pyroxene (type III) chondrules are both isotopically heavy and light. Type III chondrules have lower liquidus temperatures than type I or II chondrules [36] and therefore, they may have experienced less evaporative iron loss. However, if some type III chondrules were caught up in a high-temperature heating event that was energetic enough to melt types I and II, they may have attained superliquidus conditions and experienced enhanced evaporative loss of iron. This may explain the isotopically heavy signature of CHP-CL-3.

The fact that some Allende chondrules show significantly isotopically light compositions (ALL-CL-2, 3 and 9) compared to bulk Allende argues against a simple evaporation mechanism, unless the composition of the starting material was isotopically light. Isotopically light Fe-isotope compositions may be generated by recondensation of a light Fe-isotope enriched vapor phase produced during a heating event. Recondensation has been used previously to explain the isotopically light composition of iron in Tieschitz chondrules [7]. As previously mentioned, recondensation may be manifested by marginal enstatite [30], which could involve iron in addition to silicon. However, the absence of marginal enstatite in the three isotopically lightest chondrules (ALL-CL-2 and 3, and CHP-CL-1) may indicate that recondensation is not a viable mechanism for producing these isotopically light compositions. It is possible that recondensation of isotopically lighter material occurred prior to the last melting event, in which case the enstatite mantle (if initially present) would have been destroyed. Thus, recondensation may still be invoked as a process by which chondrules are enriched in isotopically light material. However, the possibility of isotopically light precursor material cannot not be ruled out.

In summary, although thermal history is complicated by: temporal and spatial variability in nebular conditions during chondrule melting; reworking of chondrules during multiple melting events; differences in the refractory nature of individual chondrule mineral assemblages, and parent body alteration, there is a clear indication that the more refractory type I chondrules are isotopically heavier than type II chondrules, consistent with the theory that type I chondrules have lost more iron through evaporation than type II chondrules.

6. Conclusions

This study demonstrates that iron, which is a moderately volatile element, was fractionated during the high-temperature nebular heating events that pro-

duced chondrules. In addition, Fe-isotopes appear to be a sensitive indicator of metasomatic alteration. Iron metasomatism has affected the Fe-isotope compositions in a number of ways. The relatively homogeneous Fe-isotope composition of different aliquots of interchondrule matrix, which are very similar to the bulk Allende Fe-isotope composition, indicates that either individual components were equilibrated or that heterogeneous matrix components are sufficiently fine-grained and well mixed to produce a homogeneous signature. The Fe-isotope compositions of Allende CAIs, which contain the greatest quantity of metasomatically introduced iron, are identical to the host matrix and the bulk meteorite composition. In contrast, the CAI with least bulk FeO is isotopically light. This isotopically light signature is either primary in origin and was derived from condensation of isotopically light iron in the solar nebula, or indicates that if iron was metasomatically introduced then the lighter Fe-isotopes were preferentially mobilised and deposited. The Fe-isotope composition of chondrules may have also been modified by metasomatic exchange of iron. Smaller chondrules have compositions which are very similar to matrix/bulk compositions and this suggests that these chondrules were more susceptible to equilibration with matrix iron.

Short-lived, high-temperature (chondrule forming) melting events were an intrinsic process within the protoplanetary disk. It seems likely that Fe-isotopes were fractionated during these melting episodes as chondrules span a range of Fe-isotope compositions, which are both isotopically heavy and light with respect to the host matrix and bulk compositions. This composition span is the largest to be documented thus far. The Fe-isotope compositions of chondrules do not vary with respect to texture indicating that the most recent melting event did not dictate the Fe-isotope composition. However, Fe-isotope fractionation systematics of Allende chondrules uphold the theory that type I chondrules derive from type II chondrules by melting and evaporative loss of iron and silicon as type I (FeO-poor) chondrules are mainly isotopically heavier than type II (FeO-rich) chondrules. These differences may be related to their melting history, where type I chondrules were more frequently or aggressively melted. In general, there are strong indications that the precursor solids to the chondrules were isotopically light.

Tracing the behaviour of Fe-isotopes during high-temperature, chondrule forming, events is an important way to better understand the early solar nebular environment, especially when these observations are combined with experimental and theoretical modelling of the behaviour of iron [e.g. [37]]. The effects of parent body residence on the Fe-isotopes may help us to further understand the continuing processing of matter during planetesimal/planetary formation.

Acknowledgements

References

[1] E. Mullane, S.S. Russell, M. Gounelle, V. Din, T.F.D. Mason, D. Weiss, B. Coles, Precise and accurate determination of iron isotopes by multi-collector mass spectrometry, in: G. Holland, S.D. Tanner (Eds.), Plasma Source Mass Spectrometry: Applications and Emerging Technologies, The Royal Society of Chemistry, Cambridge, 2003, pp. 351–361.

[2] E. Mullane, S.S. Russell, M. Gounelle, T.F.D. Mason, T.E. Jeffries, Iron isotope compositions in components from the Allende CV3 meteorite, Meteorit. Planet. Sci. 36 (2001) A142.

[3] E. Mullane, S.S. Russell, M. Gounelle, T.F.D. Mason, Iron isotope composition of Allende and Chainpur chondrules: effects of equilibration and thermal history, Lunar Planet. Sci. 35th, No.1027, 2003 (CD-ROM).

[4] E. Mullane, S.S. Russell, M. Gounelle, T.F.D. Mason, Iron isotope composition of Allende matrix, CAIs and chondrules, Meteorit. Planet. Sci. 38 (2003) A66.

[5] X.K. Zhu, Y. Guo, R.K. O'Nions, E.D. Young, R.D. Ash, Isotopic homogeneity of iron in the early solar nebula, Nature 412 (2001) 311–313.

[6] E. Mullane, S.S. Russell, M. Gounelle, Iron isotope fractionation within a differentiated asteroidal sample suite, Meteorit. Planet. Sci. 37 (2002) A105.

[7] K. Kehm, E.H. Hauri, C.M. O'D. Alexander, R.W. Carlson, High precision iron isotope measurements of meteoritic material by cold plasma ICP-MS, Geochim. Cosmochim. Acta 67 (2003) 2879–2891.

[8] E. Mullane, S.S. Russell, M. Gounelle, T.F.D. Mason, Relationships between HED and mesosiderite meteorites: an iron isotope perspective, Lunar Planet. Sci. 35th, No.1015, 2004 (CD-ROM).

[9] F. Poitrasson, A.N. Halliday, D.-C. Lee, S. Levasseur, N. Teutsch, Iron isotope differences between Earth, Moon, Mars and Vesta as possible records of contrasted accretion mechanisms, Earth Planet. Sci. Lett. 223 (2004) 253–266.

[10] B.A. Cohen, S. Levasseur, B. Zanda, R.H. Hewins, A.N. Halliday, Fe isotopes and the formation of chondrules, Lunar Planet. Sci. 35th, No.1656, 2004 (CD-ROM).

[11] N. Dauphas, A.M. Davis, R. Mendybaev, F.M. Richter, M. Wadhwa, P.E. Janney, N. Foley, Iron isotopic fractionation during vacuum evaporation of molten wüstite at solar compositions, Lunar Planet. Sci. 35th, No.1585, 2004 (CD-ROM).

[12] J. Völkening, D.A. Papanastassiou, Iron isotope anomalies, Astrophys. J. 347 (1989) L43–L46.

[13] B.L. Beard, C.M. Johnson, High precision iron isotope measurements of terrestrial and lunar materials, Geochim. Cosmochim. Acta 63 (1999) 1653–1660.

[14] C.M. O'D. Alexander, J. Wang, Iron isotopes in chondrules: implications for the role of evaporation during chondrule formation, Meteorit. Planet. Sci. 36 (2001) 419–428.

[15] A.N. Krot, E.R.D. Scott, M.E. Zolensky, Mineralogical and chemical modification of components in CV3 chondrites: nebular or asteroidal processing? Meteoritics 30 (1995) 748–775.

[16] G.D. Ventura, F. Bellatreccia, C.T. Williams, Zirconolite with significant REEZrNb(Mn,Fe)O$_7$ from a xenolith of the Laacher See eruptive centre, Eifel Volcanic Region, Germany, Canadian Min. 38 (2000) 57–65.

[17] X.K. Zhu, Y. Guo, R.J.P. Williams, R.K. O'Nions, A. Matthews, N.S. Belshaw, G.W. Canters, E.C. de Waal, U. Weser, B.K. Burgess, B. Salvato, Mass fractionation processes of transition metal isotopes, Earth Planet. Sci. Lett. 200 (2002) 47–62.

[18] S. Levasseur, M. Frank, J.R. Hein, A.N. Halliday, The global variation in the iron isotope composition of marine hydrogenetic ferromanganese deposits: implications for seawater chemistry? Earth Planet. Sci. Lett. 224 (2004) 91–105.

[19] M. Sharma, M. Polizzotto, A.D. Anbar, Iron isotopes in hot springs along the Juan de Fuca Ridge, Earth Planet. Sci. Lett. 194 (2001) 39–51.

[20] J.L. Skulan, B.L. Beard, C.M. Johnson, Kinetic and equilibrium Fe isotope fractionation between aqueous Fe(III) and hematite, Geochim. Cosmochim. Acta 66 (2002) 2995–3015.

[21] H.Y. McSween, Petrographic variations among carbonaceous chondrites of the Vigarano type, Geochim. Cosmochim. Acta 41 (1977) 177–179.

[22] P.R. Buseck, X. Hua, Matrices of carbonaceous chondrite meteorites, Annu. Rev. Earth Planet. Sci. 21 (1993) 255–305.

[23] M.K. Weisberg, M. Prinz, Fayalitic olivine in CV3 chondrite matrix and dark inclusions: a nebular origin, Meteorit. Planet. Sci. 33 (1998) 1087–1099.

[24] A.N. Krot, E.R.D. Scott, M.E. Zolensky, Origin of fayalitic olivine rims and lath-shaped matrix olivine in the CV3 chondrite Allende and its dark inclusions, Meteorit. Planet. Sci. 32 (1997) 31–49.

[25] G.J. MacPherson, L. Grossman, Fine-grained spinel-rich and hibonite-rich Allende inclusions, Meteoritics 17 (1982) 245–246.

[26] A.N. Krot, M.I. Petaev, M.E. Zolensky, K. Keil, E.R.D. Scott, K. Nakamura, Secondary calcium-iron rich minerals in the Bali-like and Allende-like oxidized CV3 chondrites and Allende dark inclusions, Meteorit. Planet. Sci. 33 (1998) 623–645.

[27] A.N. Krot, G.J. MacPherson, A.A. Ulyanov, M.I. Petaev, Fine-grained, spinel-rich inclusions from the reduced CV chondrites Efremovka and Leoville: I. Mineralogy, petrology, and bulk chemistry, Meteorit. Planet. Sci. 39 (2004) 1517–1553.

[28] S.S. Russell, G.R. Huss, A.J. Fahey, R.C. Greenwood, R. Hutchison, G.J. Wasserburg, An isotopic and petrologic study of calcium–aluminium-rich inclusions from CO3 meteorites, Geochim. Cosmochim. Acta 62 (1998) 689–714.

[29] A.P. Boss, A concise guide to chondrule formation models, in: R.H. Hewins, R.H. Jones, E.R.D. Scott (Eds.), Chondrules and the Protoplanetary Disk, Cambridge University Press, Cambridge, 1996, pp. 257–263.

[30] L. Tissandier, G. Libourel, F. Robert, Gas–melt interactions and their bearing on chondrule formation, Meteorit. Planet. Sci. 37 (2002) 1377–1389.

[31] C.M. O'D. Alexander, J.N. Grossman, J. Wang, B. Zanda, M. Bourot-Denise, R.H. Hewins, The lack of potassium-isotopic fractionation in Bishunpur chondrules, Meteorit. Planet. Sci. 35 (2000) 859–868.

[32] C.M. O'D. Alexander, Recycling and volatile loss in chondrule formation, in: R.H. Hewins, R.H. Jones, E.R.D. Scott (Eds.), Chondrules and the Protoplanetary Disk, Cambridge University Press, Cambridge, 1996, pp. 233–241.

[33] P.M. Radomsky, R.H. Hewins, Formation conditions of pyroxene-olivine and magnesian olivine chondrules, Geochim. Cosmochim. Acta 54 (1990) 3475–3490.

[34] R.H. Hewins, Retention of sodium during chondrule melting, Geochim. Cosmochim. Acta 55 (1991) 935–942.

[35] C.M. O'D. Alexander, Trace element distributions within ordinary chondrite chondrules: implications for chondrule formation conditions and precursors, Geochim. Cosmochim. Acta 58 (1994) 3451–3467.

[36] R.H. Hewins, P.M. Radomsky, Temperature conditions for chondrule formation, Meteoritics 25 (1990) 309–318.

[37] B.A. Cohen, R.H. Hewins, C.M. O'D. Alexander, The formation of chondrules by open-system melting of nebular condensates, Geochim. Cosmochim. Acta 68 (2004) 1661–1675.